

LETTER TO THE EDITOR

Identification of solid N₂O in interstellar ices using open JWST data

V. Karteyeva, R. Nakibov, I. Petrashkevich, M. Medvedev, and A. Vasyunin

Research Laboratory for Astrochemistry, Ural Federal University, Kuibysheva St. 48, Yekaterinburg 620026, Russia
e-mail: varvara.karteeva@urfu.ru**ABSTRACT**

Context. There are only six molecules containing N–O bond that are detected in gaseous phase in interstellar medium. One of those is nitrous oxide (N₂O), which was searched for but not found in solid form from as early as Infrared Space Observatory (ISO) mission was launched. The observational capabilities of James Webb Space Telescope (JWST) present a possibility to identify solid interstellar N₂O.

Aims. We aim to identify nitrous oxide in open JWST spectra of interstellar ices towards a sample of Class 0, 0/I and flat protostars using the relevant laboratory mixtures of N₂O-bearing interstellar ice analogues.

Methods. A set of laboratory infrared transmission spectra was obtained for the following mixtures: N₂O:CO₂=1:20, N₂O:CO=1:20, N₂O:N₂=1:20, N₂O:CO₂:CO=1:15:5, N₂O:CO₂:N₂=1:15:13 at 10–23 K. A search for N₂O in JWST NIRSpec spectra towards 50 protostars was performed by fitting the 4.44–4.47 μ m (2250–2235 cm^{-1}) NN-stretch absorption band with new laboratory mixtures of N₂O-bearing ices.

Results. We claim the first secure identification of N₂O in 16 protostars. The fitting results show that N₂O is formed predominantly within the apolar layer of the ice mantles, rich in CO, CO₂ and N₂. The abundance of solid N₂O is estimated as 0.2–2.1% relative to solid CO. We present band strengths for N₂O in the mixtures corresponding to the apolar layer. Also, an identification of the C–N stretch band at 4.42 μ m (2260 cm^{-1}) is reported, which we tentatively assign to HNCO, the simplest C–N bond carrier.

Key words. Astrochemistry, Molecular data, Methods: laboratory, Stars: protostars, ISM: abundances, ISM: molecules

1. Introduction

Nitrous oxide (N₂O) is one of the six N–O bond molecules detected in gaseous phase (McGuire 2022), important for the evolution of molecular complexity in space. While it was detected in the gaseous phase in various astronomical environments: Sgr B2 interstellar cloud (Ziurys et al. 1994; Halfen et al. 2001), protostellar binary IRAS 16293-2422 (Ligterink et al. 2018), G+0.693 molecular cloud (Rivilla et al. 2020) and the atmosphere of Mars (Villanueva et al. 2013), its solid-state counterpart — a potential tracer of nitrogen chemistry in icy grain mantles, remains elusive. The detection of solid N₂O may serve as a tracer in the formation of more complex nitrogen-bearing molecules (Fedoseev et al. 2018), act as a proxy for the presence and chemical activity of infrared-inactive molecules (N₂ and O₂) in ices (e.g. Elsila et al. 1997; Jamieson et al. 2005; Pereira et al. 2018). Nitrous oxide could provide a direct abiotic route to species of prebiotic relevance (Jamieson et al. 2005), and itself was recently proposed as a potential biosignature (Schwieterman et al. 2022).

There is a decades-long search for solid N₂O in interstellar ices. Initial investigations with the Infrared Space Observatory (ISO) yielded negative results (Ehrenfreund et al. 1997), highlighting the challenge of its identification. Laboratory studies, however, showed that N₂O is a likely product of UV-irradiated apolar ices (Elsila et al. 1997; Moore & Hudson 2003). More recent experimental works also suggested that N₂O could be a component of cold interstellar ices and could form efficiently through ion bombardment (e.g. Jamieson et al. 2005; Sicilia et al. 2012; Pereira et al. 2018) of apolar N₂-containing ices, making it a promising candidate for future observations.

N₂O can also be formed after ion bombardment of nitrous oxides as shown in experiments with NO₂:N₂O₄ mixture at 16 K and 60 K (Fulvio et al. 2019). Finally, modeling predicts N₂O to be the most abundant among nitrous oxides (N_xO_y) formed under the ion bombardment of N₂-containing ices (Queiroz et al. 2025).

The unprecedented quality of James Webb Space Telescope (JWST) data reignited the search for N₂O. Recent studies reported tentative detections in the 4.4–4.52 μ m (2272–2212 cm^{-1}) region (Nazari et al. 2024) utilizing the spectrum of pure crystalline N₂O at 70 K, and in the 7.7 μ m band towards the Ced 110 IRS4A protostar, where a spectrum of pure irradiated N₂O was used (Rocha et al. 2025). There, the first N₂O column density estimation is provided: $8.1 \times 10^{16} \text{ cm}^{-2}$ (1.8% relative to solid H₂O). Analysis of IRAS 23385+6053 also suggested a tentative assignment of a feature in the 7.7 μ m region to N₂O (Nakibov et al. 2025) based on underfitting in this region.

However, the usage of laboratory spectra of pure or irradiated N₂O ices is unreliable in context of interstellar ices complexity. N₂O is expected to be a trace component, likely embedded in CO/CO₂-rich (apolar) environments. Also, the infrared band profiles and peak positions of solid species are known to shift significantly depending on the molecular environment. Currently, the following N₂O infrared laboratory transmission spectra are available: pure N₂O in 10–70 K range (Hudson et al. 2017; Gerakines & Hudson 2020), pure N₂O at 16 K (Fulvio et al. 2009), N₂O:H₂O=1:29 at 14 K (Bergantini et al. 2022), and N₂O:CO₂=1:2 at 11 K (Pereira et al. 2018). Given the availability of quality observational JWST data the lack of relevant reference data becomes a primary obstacle to a secure identification. The fea-

ture in 2250–2235 cm^{-1} range in the open JWST data that we explore in this Letter is a candidate for interstellar solid N_2O assignment based on the NN stretching mode. This region likely contains the absorption band of the N_2O in the apolar environment (e.g. CO_2 , CO , N_2), because laboratory mixtures of N_2O in the polar layer do not match this range (see e.g. [Bergantini et al. 2022](#)). There is a number of studies that support the origin of N_2O in apolar N_2 -bearing ices: $\text{CO}:\text{N}_2$, $\text{N}_2:\text{O}_2:\text{CO}$, $\text{N}_2:\text{O}_2:\text{CO}_2:\text{CO}$ ([Elsila et al. 1997](#)), $\text{CO}:\text{N}_2$ ([Moore & Hudson 2003](#)), $\text{N}_2:\text{CO}_2$ ([Jamieson et al. 2005](#)), $\text{CO}:\text{N}_2$ ([Sicilia et al. 2012](#)), $\text{N}_2:\text{O}_2$ ([Lo et al. 2018](#)).

In this Letter, we present the first reliable identification of solid N_2O in interstellar ices. We achieve this by combining the unparalleled sensitivity and resolution of JWST with a dedicated laboratory study of N_2O in the apolar environment. Our survey of 50 protostars of variable classes and masses available in the MAST database revealed clear spectroscopic signatures of N_2O in 16 sources, allowing us to derive its column density and establish first observational constraints on its environment in interstellar ice.

2. Experimental setup and methods

The transmission laboratory spectra used for N_2O identification were obtained using the Ice Spectroscopy Experimental Aggregate (ISEAge), a cryogenic ultra-high vacuum setup described in detail in [Ozhiganov et al. \(2024\)](#). Briefly, ISEAge setup allows for the production and study of the interstellar ice analogues. The base pressure in the chamber prior to experiments is 2×10^{-10} mbar, the temperature of the Ge substrate can be set and held within 6.7–305 K range. Transmission laboratory infrared (IR) spectra are obtained with the Thermo Scientific Nicolet iS50 FTIR spectrometer operated within a 4000–630 cm^{-1} (2.5–15.9 μm) range with 1 cm^{-1} resolution. The ices were deposited via the ‘background deposition’ technique ([Accolla et al. 2011](#); [Fedoseev et al. 2015](#); [Rachid et al. 2021, 2022](#); [Kruckiewicz et al. 2024](#); [Satorre et al. 2025](#)). The individual deposition rates are calibrated using Stanford Research Systems RGA200 quadrupole mass spectrometer (QMS) in combination with IR spectroscopy via the calibration curves, which we obtained following [Slavicinska et al. \(2023\)](#).

The ices were grown on a Ge substrate cooled down to 10 ± 0.1 K. The N_2O deposition rate was calibrated using the band strength of 5.891×10^{-17} cm for ν_3 mode at 10 K taken from [Hudson et al. \(2017\)](#). In all the experiments pure N_2O was introduced into the main UHV chamber at the desired fixed deposition rate through the first leak valve. Simultaneously, second gas or pre-calibrated gas mixture was introduced into the main chamber through the second independent leak valve. The QMS signal is continuously monitored during the depositions to ensure that the deposition rate is consistent with the calibration curve values. The compositions of the deposited ice mixtures were verified by examining the features in IR spectra. Co-depositions continued for 120 minutes with N_2O deposition rate fixed at 2.95×10^{12} $\text{cm}^{-2} \text{s}^{-1}$. This resulted in a total N_2O column density of 2×10^{16} cm^{-2} . Afterwards, the ice was warmed up at a rate of 0.5 K per minute. During the warm up the infrared laboratory spectra were recorded every 45 seconds (averaging of 32 scans). In this Letter we present the transmission laboratory spectra of N_2O absorption in the apolar environment at 10 K and 23 K for the first time: $\text{N}_2\text{O}:\text{CO}_2=1:20$, $\text{N}_2\text{O}:\text{CO}=1:20$, $\text{N}_2\text{O}:\text{N}_2=1:20$, $\text{N}_2\text{O}:\text{CO}_2:\text{CO}=1:15:5$, $\text{N}_2\text{O}:\text{CO}_2:\text{N}_2=1:15:13$. The N_2O absorption bands were isolated via baseline correction for further use.

The compounds used are as follows: N_2O (99.999 %, BK-Grypp), CO (99.9999 %, Ugra-PGS), CO_2 (99.9999 %, Ugra-PGS), N_2 (99.9999 %, Ugra-PGS). Gaseous N_2O , CO , CO_2 and N_2 are introduced directly into the dosing lines from the commercially acquired gas bottles.

3. Observations and fitting procedure

For this Letter we focused on detecting N_2O by its most prominent ν_3 absorption band at $\sim 4.45 \mu\text{m}$. The $7.77 \mu\text{m}$ band (ν_1) is about four times less intense and was not analyzed due to insufficient signal-to-noise ratio in this region.

We surveyed the MAST¹ database for protostars observed with JWST Near-Infrared Spectrometer (NIRSpec) and compiled an initial list of 50 sources (MAST DOI: [10.17909/tg2a-kv41](#)). NIRSpec uses G395M/G395H modes with the spectral resolution of ~ 1000 and ~ 2700 , respectively, and covers 2.87–5.27 μm range. The science data with the level 3 pipeline calibration was used for this study (calibration pipeline described by [Greenfield & Miller 2016](#); [Bushouse et al. 2024](#); [van Gelder et al. 2024](#)). We manually examined each source and searched for the apertures with detectable N_2O features based on our laboratory reference spectra. The search was challenged by the presence of gaseous CO emission lines that overlapped with the region of interest and, therefore, sources were classified into three groups:

- + Sources in which we were able to identify an aperture with N_2O features that had none or weak overlap with CO emission,
- + Sources in which we were able to identify an aperture with N_2O features that had overlap with CO emission, but the emission could be masked without causing severe distortions to the spectrum,
- Sources in which we were not able to identify an aperture with N_2O features due to strong CO emission and/or low signal-to-noise ratio.

The search yielded 16 sources (MAST DOI: [10.17909/sg05-m334](#)) in which we selected the apertures with minimal distortions in the N_2O region aiming for a the secure detection claim. In four objects the N_2O feature was recovered from gaseous CO lines. For these sources we provide an additional aperture with a clear N_2O feature. The intensity maps and chosen apertures are presented in Appendix A. The aperture parameters are presented in Table C.1 in Appendix C.

Then, the laboratory spectra were prepared for the fitting procedure by subtracting the continuum and converting them to optical depth. If required, we masked the gaseous CO emission lines. Details are presented in Appendix B. In some of the laboratory spectra the N_2O feature overlaps with a feature in 2280–2250 cm^{-1} (4.39–4.44 μm) region, commonly associated with CN-stretch band, e.g. isocyanic acid (HNCO), acetonitrile (CH_3CN). The CN-stretch region also contained a gaseous emission doublet (H_2 , [Nazari et al. 2024](#)), spanning in 2270–2265 cm^{-1} range, which hindered the identification of the exact carrier. Thus, we tentatively assigned it to HNCO as it is the simplest CN-bearing molecule in this spectral region. A Gaussian function was included in the fit to cover the 2280–2250 cm^{-1} feature, which resolved the overlapped bands. We also fitted Gaussian functions to estimate column densities of CO , $^{13}\text{CO}_2$ and

¹ MAST database: <https://mast.stsci.edu/portal/Mashup/Clients/Mast/Portal.html>

OCN⁻. The ¹²CO₂ absorption band was not analyzed due to saturation in the observational data. We also note that the profile of intense solid CO feature at 4.67 μ m towards protostars can be impacted by grain shape effects (see, e.g. Pontoppidan et al. 2003, and references therein). However, this issue is not explored in this Letter.

The fitting was performed in two stages. For the first stage, we used the laboratory spectra of N₂O in apolar environment: mixtures with CO, CO₂ and N₂, see Fig. 1. The objects in our study are protostars, which are likely to have a temperature gradient in their inner regions. However, we lack detailed constraints on the physical structure of these sources. The considered observational spectra exhibit strong solid CO absorption feature at 4.67 μ m. Also, the N-bearing ices we are investigating have relatively low sublimation temperatures. Finally, laboratory experiments proved the possibility of N₂O formation in N₂-containing ices at low temperatures (e.g., Fedoseev et al. 2018). We therefore assume that the fitted spectral features originate from cold ices residing in cold envelopes of protostars. Consequently, we use laboratory ice spectra obtained at temperatures below the sublimation point of N₂ (23 K) to analyze the observations. Each ice mixture spectrum is available at 35 discrete temperature points, spaced at even intervals of \sim 0.4 K. For each source, we performed a fit at each of these 35 temperatures T_i by modeling the observed spectral feature with a linear combination of laboratory spectra of different mixtures—all taken at that same T_i —plus an HNCO Gaussian function, minimizing χ^2 :

$$\chi^2(T_i) = \sum_{j=1}^{N_{obs}} \frac{(\tau_{obs}^j - \tau_{lab}^j(T_i))^2}{\sigma_j^2}, \quad (1)$$

where τ_{obs} is the optical depth of the observational spectrum, $\tau_{lab}(T_i)$ is the optical depth of a fitted linear combination of laboratory spectra and HNCO Gaussian at 2280–2250 cm^{-1} . T_i is the temperature of the fitted combination, N_{obs} is a number of points in the fitted segment of the observational spectrum and σ_j is the point-wise standard deviation of the observational spectrum. A sliding-window smoothed curve (12–16 points, locally estimated weighted scatterplot smoothing, Cleveland 1979) was subtracted from the original optical depth spectrum to estimate σ_i from the residuals. From these 35 fits across the 10–23 K range, we then selected the overall best-fit spectrum for each source. Following Avni (1976), the error of temperature estimates were obtained from $\chi^2(T_i)$ line with $\Delta\chi^2 = 1$ ($\alpha = 68\%$). Column density errors were estimated as the best-fit uncertainty. The band strengths of N₂O in mixtures were estimated from band area measurements based on value from Hudson et al. (2017) (see band strengths in Table C.2).

In the second stage the fitted spectrum was subtracted from the observational spectrum because the Gaussian in the 2280–2250 cm^{-1} region overlaps with the ¹³CO₂ feature. Then, three Gaussian functions were fitted to the residual spectrum to estimate column densities of CO, OCN⁻ and ¹³CO₂. As in the first stage, column density errors were estimated as the best fit uncertainty.

4. Results and Discussion

In Fig. 1 we present the new laboratory infrared transmission spectra of N₂O-bearing mixtures in the apolar environment along with pure N₂O and N₂O:H₂O mixture at 10 K and 23 K. The spectra obtained at intermediate temperatures are not shown because the shapes of N₂O features vary smoothly in the 10–

23 K range. The 4.45 μ m (ν_3) feature in apolar environment displays a significant blueshift, compared to both pure N₂O and N₂O:H₂O mixture. The highest blueshift of 28 cm^{-1} relative to pure N₂O is observed for N₂O:CO₂=1:20 mixture. Ternary mixtures with CO₂ and CO/N₂ produce a broad N₂O feature, limited by the peak positions observed for binary mixtures with CO₂ and CO/N₂ at a ratio of 1:20. The structure of N₂O feature in ternary mixtures clearly indicates the presence of CO/N₂- and CO₂-associated components. Thus, the position and shape of the feature are sensitive to the ice composition. In summary, the N₂O absorption band in the apolar environment spans in about 2250–2235 cm^{-1} range with composition-dependent line shape.

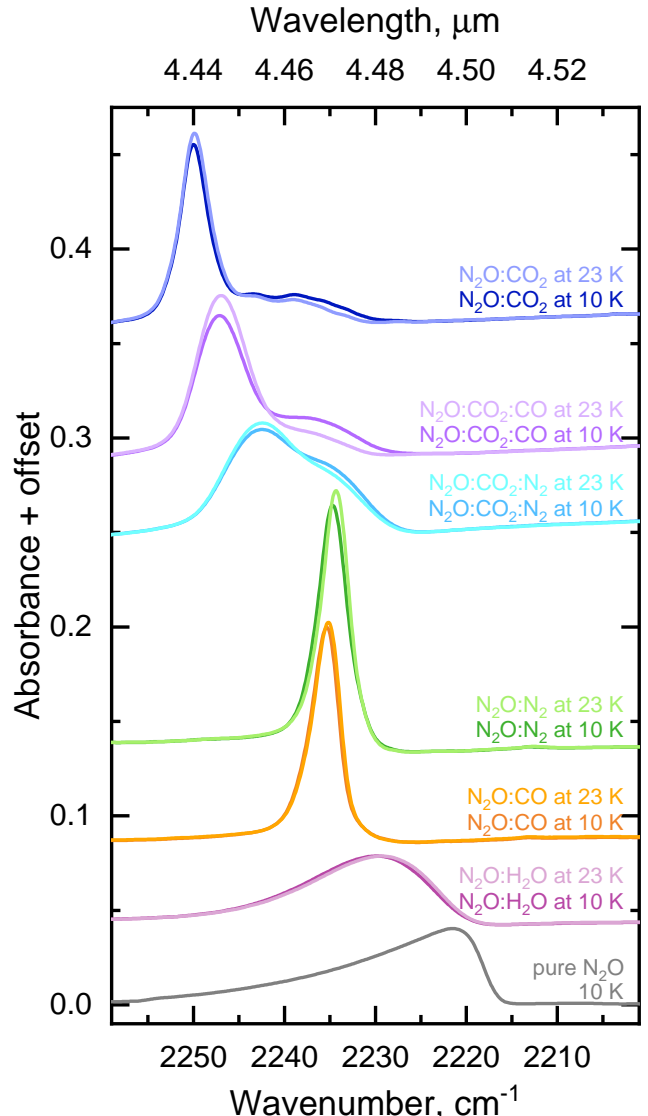


Fig. 1: The ν_3 mode of N₂O in pure N₂O, N₂O:H₂O=1:20 and nitrous oxide in astrochemically relevant matrices corresponding to the apolar layer of ice mantles N₂O:CO=1:20, N₂O:N₂=1:20, N₂O:CO₂:N₂=1:15:13, N₂O:CO₂:CO=1:15:5, N₂O:CO₂=1:20. Spectra are displayed only for the lowest and the highest temperatures considered in this study.

In Fig. D.1 the observed spectra of N₂O-related feature for 20 apertures in 16 protostars are shown along with best fitting results. As can be seen from comparison with Fig. 1, the spec-

tral feature of $\text{N}_2\text{O}:\text{H}_2\text{O}$ mixture positioned at 2230 cm^{-1} falls outside the observed features. All derived temperatures and column densities are listed in Table C.1. In all observed sources, the JWST spectra were fitted with the ice mixtures corresponding to the apolar layer of the ice mantles. The derived N_2O column densities relative to solid CO are in the range of 0.2–2.1%. Assuming a typical CO abundance relative to H_2O in a range of 10–30%, we estimate the N_2O abundance with respect to H_2O to be in the range of 0.02–0.84%. The $2280\text{--}2250\text{ cm}^{-1}$ band was tentatively assigned to the C–N stretch absorption band of HNCO. It is the simplest CN-stretch mode carrier that commonly appears with N_2O in the irradiation experiments (see e.g. Fedoseev et al. 2018). Due to the H_2 emission in $2270\text{--}2265\text{ cm}^{-1}$ range we constrained the HNCO peak position to $2260\pm2\text{ cm}^{-1}$, which aligns with the 2260 cm^{-1} HNCO feature reported in Fedoseev et al. (2018). We note that CH_3CN or $\text{C}_2\text{H}_5\text{CN}$ are other possible candidates for this region (Nazari et al. 2024). The column densities obtained in this work for $^{13}\text{CO}_2$, OCN^- are in agreement with values previously published in literature, see Appendix C for more details.

The detection of N_2O in the apolar layer is in agreement with the laboratory studies on the irradiation of N_2 -bearing ices (e.g. Elsila et al. 1997; Lo et al. 2018). There are both observational and chemical reasons for non-detection of N_2O in the $\sim 2230\text{ cm}^{-1}$ region, that corresponds to N_2O embedded in H_2O . In observational data for this region the gaseous CO interference is stronger, which lowers the quality of the data and complicates the data selection. The chemical reason is the limited availability of N_2O key precursor, N_2 , in H_2O -dominated ices (Hudson 2018). Interestingly, 8 of the 16 sources from the sample are the so-called HOPS sources in Orion A. Notably, this region is a subject to high UV background irradiation (Peeters et al. 2024), which further supports the irradiation-driven pathways of N_2O formation in interstellar ices.

Acknowledgements. This work is based on observations made with the NASA/ESA/CSA James Webb Space Telescope. The data were obtained from the Mikulski Archive for Space Telescopes at the Space Telescope Science Institute, which is operated by the Association of Universities for Research in Astronomy, Inc., under NASA contract NAS 5-03127 for JWST. We would like to thank Gleb Fedoseev and Vadim Krushinsky for assembling, calibrating and launching the ISEAge setup, and to Olga Russkikh for helpful discussions during manuscript revision. We thank the anonymous reviewer for their insightful comments that helped us to improve the manuscript. This research work is funded by the Russian Science Foundation via 23-12-00315 agreement.

Furlan, E., Fischer, W. J., Ali, B., et al. 2016, ApJS, 224, 5
 Gerakines, P. A. & Hudson, R. L. 2020, ApJ, 901, 52
 Gerakines, P. A., Materese, C. K., & Hudson, R. L. 2025, MNRAS, 537, 2918
 Greenfield, P. & Miller, T. 2016, A&C, 16, 41
 Halfen, D., Apponi, A., & Ziurys, L. 2001, ApJ, 561, 244
 Hudson, R., Loeffler, M., & Gerakines, P. 2017, JChPh, 146
 Hudson, R. L. 2018, ApJ, 867, 160
 Jamieson, C. S., Bennett, C. J., Mebel, A. M., & Kaiser, R. I. 2005, ApJ, 624, 436
 Kruczakiewicz, F., Dulieu, F., Ivlev, A. V., et al. 2024, A&A, 686, A236
 Launhardt, R., Stutz, A. M., Schmiedeke, A., et al. 2013, A&A, 551, A98
 Ligterink, N. F. W., Calcutt, H., Coutens, A., et al. 2018, A&A, 619, A28
 Lo, J.-I., Chou, S.-L., Peng, Y.-C., et al. 2018, ApJ, 864, 95
 McGuire, B. A. 2022, ApJS, 259, 30
 Moore, M. & Hudson, R. 2003, Icarus, 161, 486
 Nakibov, R., Karteyeva, V., Petrushkevich, I., et al. 2025, ApJL, 978, L46
 Nazari, P., Rocha, W., Rubinstein, A., et al. 2024, A&A, 686, A71
 Ortiz-León, G. N., Loinard, L., Dzib, S. A., et al. 2018, ApJ, 865, 73
 Ozhiganov, M., Medvedev, M., Karteyeva, V., et al. 2024, ApJL, 972, L10
 Peeters, E., Habart, E., Berné, O., et al. 2024, A&A, 685, A74
 Pereira, R., de Barros, A., Fulvio, D., et al. 2018, MNRAS, 478, 4939
 Pontoppidan, K. M., Fraser, H. J., Dartois, E., et al. 2003, A&A, 408, 981
 Queiroz, L., Silva, J., Ferrão, L., & Pilling, S. 2025, MNRAS, staf225
 Rachid, M. G., Brunken, N., de Boe, D., et al. 2021, A&A, 653, A116
 Rachid, M. G., Rocha, W. R. M., & Linnartz, H. 2022, A&A, 665, A89
 Riaz, B., Martín, E. L., Bouy, H., & Tata, R. 2009, ApJ, 700, 1541
 Rivilla, V. M., Martín-Pintado, J., Jiménez-Serra, I., et al. 2020, ApJL, 899, L28
 Rocha, W., McClure, M., Sturm, J., et al. 2025, A&A, 693, A288
 Satorre, M. Á., Escrivano, B., Santonja, C., et al. 2025, A&A, 703, A89
 Schwierman, E. W., Olson, S. L., Pidhorodetska, D., et al. 2022, ApJ, 937, 109
 Sicilia, D., Ioppolo, S., Vindigni, T., Baratta, G. A., & Palumbo, M. E. 2012, A&A, 543, A155
 Slavicinska, K., Rachid, M. G., Rocha, W. R. M., et al. 2023, A&A, 677, A13
 Smith, Z. L., Dickinson, H. J., Fraser, H. J., et al. 2025, NatAs, 9, 883
 Tobin, J. J., Looney, L. W., Li, Z.-Y., et al. 2016, ApJ, 818, 73
 Tobin, J. J., Offner, S. S. R., Kratter, K. M., et al. 2022, ApJ, 925, 39
 van Gelder, M. L., Ressler, M. E., van Dishoeck, E. F., et al. 2024, A&A, 682, A78
 Villanueva, G., Mumma, M., Novak, R., et al. 2013, Icarus, 223, 11
 Ziurys, L., Apponi, A., Hollis, J., & Snyder, L. 1994, ApJ, 436, L181

References

Accolla, M., Congiu, E., Dulieu, F., et al. 2011, PCCP, 13, 8037
 Avni, Y. 1976, ApJ, 210, 642
 Bergantini, A., de Barros, A. L. F., Toribio, N. N., et al. 2022, JPCA, 126, 2007
 Bouilloud, M., Fray, N., Bénilan, Y., et al. 2015, MNRAS, 451, 2145
 Brunken, N. G. C., Boogert, A. C. A., van Dishoeck, E. F., et al. 2025, ESC, 9, 1992
 Brunken, N. G. C., van Dishoeck, E. F., Slavicinska, K., et al. 2024, A&A, 692, A163
 Bushouse, H., Eisenhamer, J., Dencheva, N., et al. 2024, JWST Calibration Pipeline
 Chen, H.-R. V., Keto, E., Zhang, Q., et al. 2016, ApJ, 823, 125
 Cleveland, W. S. 1979, JASA, 74, 829
 Ehrenfreund, P., d'Hendecourt, L., Dartois, E., et al. 1997, Icarus, 130, 1
 Elsila, J., Allamandola, L. J., & Sandford, S. A. 1997, ApJ, 479, 818
 Fedoseev, G., Ioppolo, S., Zhao, D., Lamberts, T., & Linnartz, H. 2015, MNRAS, 446, 439
 Fedoseev, G., Scirè, C., Baratta, G. A., & Palumbo, M. E. 2018, MNRAS, 475, 1819
 Fulvio, D., Baratta, G. A., Sivaraman, B., et al. 2019, MNRAS, 483, 381
 Fulvio, D., Sivaraman, B., Baratta, G. A., Palumbo, M. E., & Mason, N. J. 2009, AcSpA, 72, 1007

Appendix A: Apertures

The intensity maps at 4.4 μ m and selected apertures for the sources described in this Letter are displayed in Fig. A.1. Gaseous CO lines were masked in spectra extracted from the white apertures. Spectra extracted from the green apertures contained clean N₂O features as is. For B1-c a ring aperture was used to avoid gaseous lines towards the center. The data on the sources and the aperture parameters are listed in Table C.1.

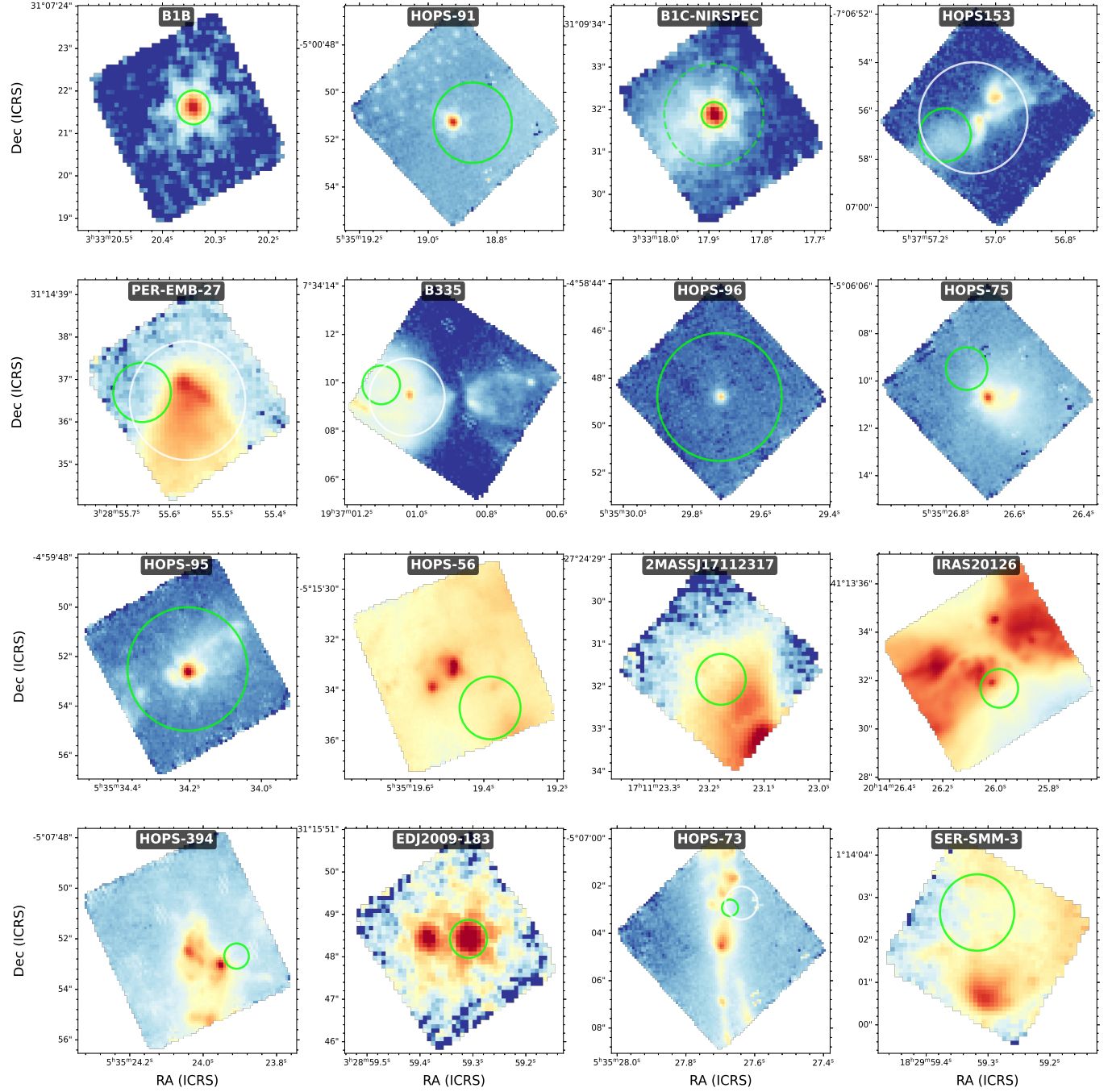


Fig. A.1: Intensity maps at 4.4 μ m with the apertures chosen for the fit. Aperture centers and diameters are listed in Table C.1.

Appendix B: Baselines

This section contains original and processed spectra with masked gaseous lines. The anchor points for local continuum subtraction were selected in absorption-free regions to isolate two groups of overlapping features: ¹³CO₂, HNCO, N₂O and OCN⁻, CO. Most of the points were chosen in the following ranges: 2325–2290 cm^{-1} , between ¹²CO₂ and ¹³CO₂; 2230–2185 cm^{-1} , between the proposed N₂O and OCN⁻ feature; 2125–2065 cm^{-1} , next to the CO feature. In a few cases we included additional points outside

these ranges to ensure the conservative estimation of local continuum and peak areas. A polynomial function, with a degree ranging from three to five, was selected to model the continuum. The spectra with the selected continua are shown in Fig. B.1.

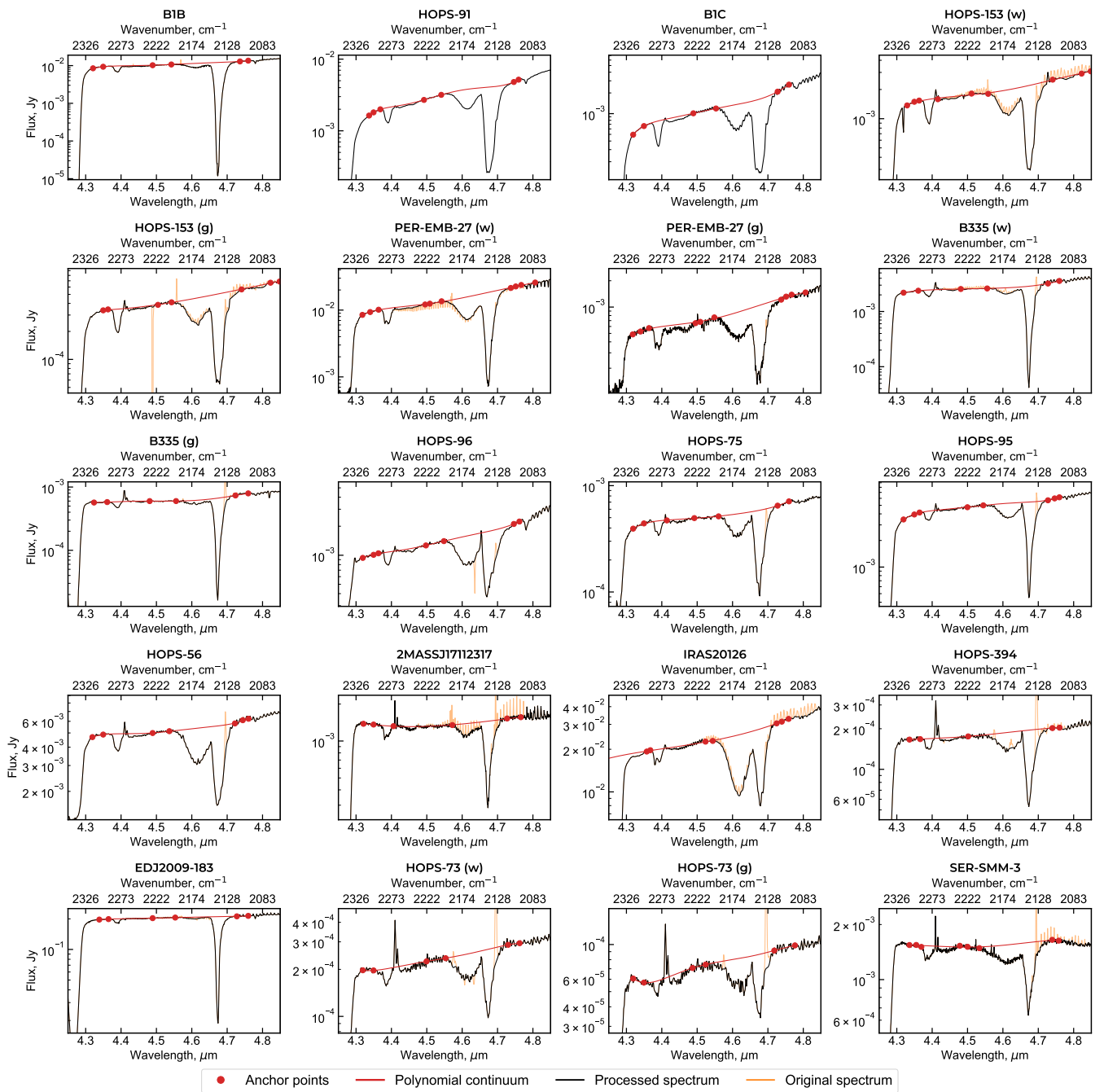


Fig. B.1: Raw and processed observational spectra with fitted polynomial continuum. Anchor points are represented with red dots, fitted continuum with red line. Original and processed observational spectra are shown with orange and black lines, respectively.

Appendix C: Sources and column densities

The sources and apertures' parameters along with the derived column densities are listed in Table C.1. In this work we estimated the column density of $^{13}\text{CO}_2$ to be in the range of $(1.3 - 11) \times 10^{16} \text{ cm}^{-2}$. This range is consistent with $^{13}\text{CO}_2$ column density range of $(1.2 - 8.1) \times 10^{16} \text{ cm}^{-2}$ presented in Brunken et al. (2024), $2.3 \times 10^{16} \text{ cm}^{-2}$ value for IRAS 20126 and $2.8 \times 10^{16} \text{ cm}^{-2}$ for Per-emb 35 presented in Brunken et al. (2025). Brunken et al. (2024) also presents individual column densities for B1-b, B1-c, EDJ2009-183, SER-SMM-3, PER-EMB-27 are $2.6 \times 10^{16} \text{ cm}^{-2}$, $7.1 \times 10^{16} \text{ cm}^{-2}$, $0.58 - 0.7 \times 10^{16} \text{ cm}^{-2}$, $2 \times 10^{16} \text{ cm}^{-2}$ and $5.9 \times 10^{16} \text{ cm}^{-2}$, respectively. These values are lower than ones derived in this work, which is explained by difference in band strengths used.

Column density values for CO obtained in this work are in $(64.5 - 464) \times 10^{16} \text{ cm}^{-2}$ range, consistent with, for example, $6.6 \times 10^{17} \text{ cm}^{-2}$ for Ced 110 IRS4B: (Rocha et al. 2025) and $(20 - 365) \times 10^{16} \text{ cm}^{-2}$ for Cha I (Smith et al. 2025). Brunken et al. (2024) also presents individual CO column densities for B1-b, B1-c, EDJ2009-183, SER-SMM-3, PER-EMB-27: $410 \times 10^{16} \text{ cm}^{-2}$, $500 \times 10^{16} \text{ cm}^{-2}$, $(94 - 100) \times 10^{16} \text{ cm}^{-2}$, $120 \times 10^{16} \text{ cm}^{-2}$ and $340 \times 10^{16} \text{ cm}^{-2}$, respectively. These values are similar with the ones presented in this Letter, given the difference in chosen apertures. Derived OCN⁻ values are in range of $(0.6 - 14.6) \times 10^{16} \text{ cm}^{-2}$, in agreement with $2.6 \times 10^{16} \text{ cm}^{-2}$ for IRAS 16253, $5.0 \times 10^{16} \text{ cm}^{-2}$ for B335, $6.8 \times 10^{16} \text{ cm}^{-2}$ for HOPS 153, $16 \times 10^{16} \text{ cm}^{-2}$ for HOPS 370 (Nazari et al. 2024), and $9.2 \times 10^{16} \text{ cm}^{-2}$ for Ced 110 IRS4A (Rocha et al. 2025). To the best of our knowledge, there are currently no HNCO estimates in the literature. The band strengths for N₂O at 10 K in various environments were calculated based on 10 K band strength value from Hudson et al. (2017). The values obtained are listed in the Table C.2.

Table C.1: Parameters of the studied objects and quantities derived from the fit.

Source	Class	Coordinates	D ''	T (K) N ₂ O	Column densities (N), $\times 10^{16} \text{ cm}^{-2}$				R %	
					N ₂ O	HNCO	¹³ CO ₂	OCN ⁻	CO	
B1-b ^a	0	3 ^h 33 ^m 20.3415 ^s 31°7'21.6139"	0.8	12 ⁺⁶ ₋₂	1.1±0.1	1.3±0.1	5.0±1.0	4.7±1.0	464±7	0.2
HOPS-91 ^b	0	5 ^h 35 ^m 18.8710 ^s -5°0'51.2845"	3.4	23 ⁺⁰ ₋₁	0.8±0.2	1.2±0.2	7.0±1.0	10.0±0.8	387±8	0.2
B1-c ^a	0/I	3 ^h 33 ^m 17.8906 ^s 31°9'31.8779"	0.6 2.4 ^g	23 ⁺⁰ ₋₄	2.2±0.2	2.1±0.3	11.0±0.9	13.3±0.7	385±7	0.6
HOPS-153 ^b (w) ^h	0	5 ^h 37 ^m 57.0635 ^s -7°6'56.2890"	4.6	18 ⁺² ₋₂	1.6±0.3	0.4±0.2	8.3±0.7	10.1±0.6	261±6	0.6
HOPS-153 ^b (g)	0	5 ^h 37 ^m 57.1443 ^s -7°6'56.9967"	2.2	12 ⁺¹¹ ₋₂	1.0±0.2	0.6±0.2	7.9±0.7	11.2±0.6	296±6	0.4
PER-EMB-27 ^a (w)	0	3 ^h 28 ^m 55.5662 ^s 31°14'36.4986"	2.8	11 ⁺⁴ ₋₁	1.3±0.1	1.9±0.1	8.1±0.7	14.6±0.5	295±4	0.4
PER-EMB-27 ^a (g)	0	3 ^h 28 ^m 55.6521 ^s 31°14'36.6958"	1.4	11 ⁺² ₋₁	4.4±0.3	2.9±0.4	8.9±0.5	13.1±0.4	261±4	1.7
B335 ^c (w)	0	19 ^h 37 ^m 1.0285 ^s 7°34'9.4052"	3.2	23 ⁺⁰ ₋₁	1.3±0.1	—	4.0±1.0	4.2±1.0	284±8	0.4
B335 ^c (g)	0	19 ^h 37 ^m 1.1022 ^s 7°34'9.9127"	1.6	23 ⁺⁰ ₋₁	0.7±0.1	—	3.0±1.0	2.4±0.9	236±7	0.3
HOPS-96 ^b	0	5 ^h 35 ^m 29.7202 ^s -4°58'48.7875"	5.4	23 ⁺⁰ ₋₁	1.6±0.3	0.3±0.1	4.0±1.0	12.6±1.0	212±10	0.8
HOPS-75 ^b	0	5 ^h 35 ^m 26.7402 ^s -5°6'9.4794"	1.8	23 ⁺⁰ ₋₃	1.2±0.5	0.7±0.5	4.2±0.6	7.8±0.4	193±4	0.6
HOPS-95 ^b	0	5 ^h 35 ^m 34.2059 ^s -4°59'52.5012"	5	23 ⁺⁰ ₋₃	0.7±0.2	0.2±0.1	4.0±1.0	6.8±0.8	178±6	0.4
HOPS-56 ^b	0	5 ^h 35 ^m 19.3829 ^s -5°15'34.6982"	2.48	22 ⁺¹ ₋₆	1.0±0.1	0.6±0.1	4.2±0.4	10.4±0.4	162±3	0.6
2MASSJ17112317 ^e	0/I	17 ^h 11 ^m 23.1784 ^s -27°24'31.8296"	1.2	23 ⁺⁰ ₋₁	1.2±0.1	—	3.2±0.4	3.5±0.3	124±2	1.0
IRAS20126 ^d	0/I	20 ^h 14 ^m 25.9868 ^s 41°13'31.6776"	1.6	23 ⁺⁰ ₋₁₀	1.0±0.2	0.3±0.1	3.7±0.4	17.9±0.3	130±2	0.8
HOPS 394 ^b	0	5 ^h 35 ^m 23.9090 ^s -5°7'52.6847"	1	20 ⁺³ ₋₁₀	1.0±0.4	0.7±0.6	2.5±0.6	5.8±0.6	128±5	0.8
EDJ2009-183 ^a	flat	3 ^h 28 ^m 59.3083 ^s 31°15'48.4229"	0.9	23 ⁺⁰ ₋₂	0.19±0.02	—	1.3±0.3	0.6±0.3	110±2	0.2
HOPS-73 ^b (w)	0	5 ^h 35 ^m 27.6386 ^s -5°7'2.7197"	1.4	11 ⁺¹² ₋₁	2.0±0.5	0.8±0.4	3.7±0.6	7.7±0.5	95±4	2.1
HOPS-73 ^b (g)	0	5 ^h 35 ^m 27.6716 ^s -5°7'2.9227"	0.7	23 ⁺⁰ ₋₁₃	2.5±0.6	1.2±0.8	2.4±0.7	9.6±0.8	83±6	3.0
SER-SMM-3 ^f	0	18 ^h 29 ^m 59.3176 ^s 1°14'2.6471"	1.8	23 ⁺⁰ ₋₁	0.5±0.4	1.0±0.4	3.0±0.3	7.7±0.3	64±2	0.6

Notes. For each source listed are class, coordinates, diameter of the aperture (D), N₂O temperature, column density for N₂O, HNCO, ¹³CO₂, OCN⁻, CO and N₂O abundance with respect to CO (R). Protostar classes are taken from: ^(a) Tobin et al. (2016) ^(b) Furlan et al. (2016); Tobin et al. (2022) ^(c) Launhardt, R. et al. (2013) ^(d) Chen et al. (2016) ^(e) Riaz et al. (2009) ^(f) Ortiz-León et al. (2018) ^(g) For B1-c the ring aperture is used, inner and outer diameters are listed. ^(h) W (white) and g (green) indicate the color of the aperture in Fig. A.1.

Table C.2: The list of used absorption band strength values for fit.

Molecule	Peak Position (cm ⁻¹)	Band Strength (cm)	References
N ₂ O:CO	2235.4	4.9×10 ⁻¹⁷	this work
N ₂ O:CO ₂	2250	4.7×10 ⁻¹⁷	this work
N ₂ O:CO ₂ :CO	2245.9	5.2×10 ⁻¹⁷	this work
N ₂ O:CO ₂ :N ₂	2242.6	6.8×10 ⁻¹⁷	this work
N ₂ O:N ₂	2234.7	5.8×10 ⁻¹⁷	this work
HNCO	2255	9.79×10 ⁻¹⁷	Gerakines et al. (2025)
¹³ CO ₂	2283	6.8×10 ⁻¹⁷	Bouilloud et al. (2015)
OCN ⁻	2170	1.51×10 ⁻¹⁶	Gerakines et al. (2025)
CO	2139	1.12×10 ⁻¹⁷	Bouilloud et al. (2015)

Appendix D: Fitting results

The observational spectra for the selected sample of sources, fitted N_2O -bearing laboratory spectra and HNCO Gaussians are shown in Fig. D.1.

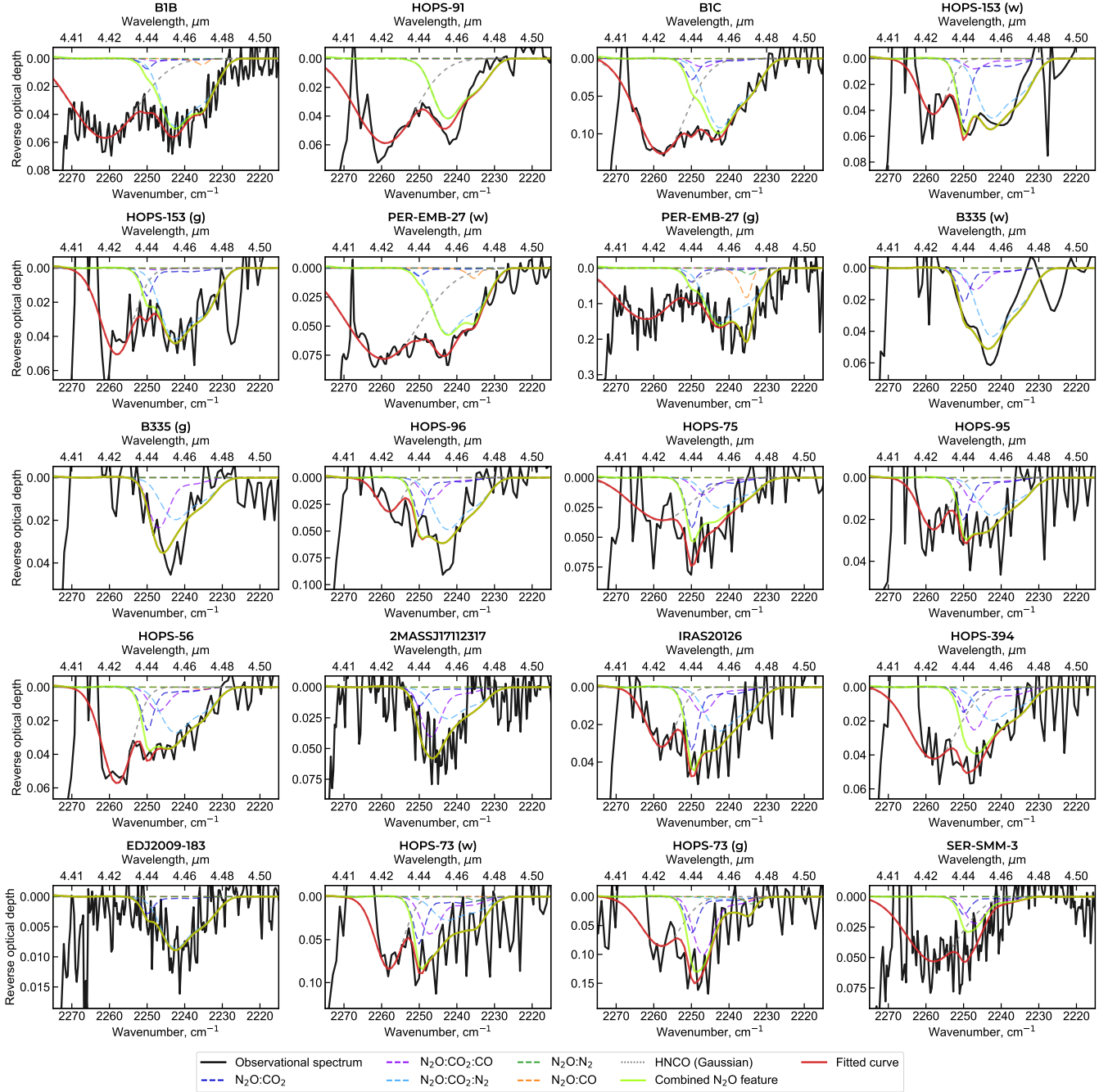


Fig. D.1: Observational data at $4.45\text{ }\mu\text{m}$, fitted curves and Gaussian function for HNCO. Black line represents the observational spectra, dashed — laboratory spectra of N_2O in apolar environment, short dashed — HNCO Gaussian, green — combined N_2O feature, and red — full fitted curve.